energy&fuels

pubs.acs.org/EF

Article

Designing Self-Assembled Dye−Redox Shuttle Systems via Interfacial π-Stacking in Dye-Sensitized Solar Cells for Enhanced Low Light Power Conversion

Dinesh Nugegoda, Shrabanti Bhattacharya, Leigh Anna Hunt, Samantha J. Schwartz, Zane H. Turner, Nathan I. Hammer,* Jonah W. Jurss,* and Jared H. Delcamp*

Cite This: *Energy Fuels* 2022, 36, 7075−7086

Read Online

ACCESS | Metrics & More | Article Recommendations | Supporting Information

ABSTRACT: Productive electron transfer in dye-sensitized solar cells is critically important to achieving high-performing solar cell devices. In this regard, increasing the electron transfer rate between the dye and redox shuttle by noncovalent self-assembly of the dye and redox shuttle via π-stacking interactions is considered. In this study, a dye with a pyrene-based donor group (**SS1**) was synthesized and tested with two terpyridine-based redox shuttles. The $[Co(tpy^{pyr})_2]^{3+/2+}$ redox shuttle (RS) has a pyrene substitution that allows for stronger π-stacking via pyrene−pyrene interactions than a benchmark unsubstituted terpyridine-ligated redox shuttle ($[Co(tpy)_2]^{3+/2+}$). DSC devices were fabricated with the dye and each redox shuttle, and the performances were evaluated by using current density−voltage (*J*−*V*), incident photon-to-current conversion efficiency (IPCE), small modulated photovoltage transient (SMPVT), photocurrent dynamic, and transient absorption measurements. Results show that pyrene groups on both the dye and RS increase the rate of dye regeneration and slow the recombination rate. A 22.8% power conversion efficiency (versus 12.4% for the system with no pyrene on the redox shuttle) under fluorescent lighting conditions is observed.

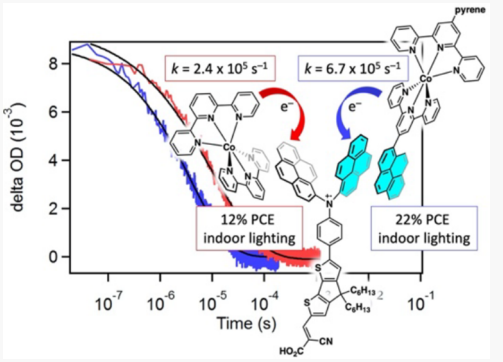

INTRODUCTION

Dye-sensitized solar cells (DSCs) are a promising photovoltaic technology,[1−3] especially with regard to low light applications[4−7] such as with indoor light recycling used to power Internet of Things devices,[8−10] underwater applications,[11] building integrated photovoltaics,[12−14] and in tandem or multijunction devices.[15−19] DSCs operate by (1) photoexcitation of a dye, (2) injection of an electron into a semiconductor such as TiO_2, (3) regeneration of the neutral dye from the cationic state by electron transfer from a redox shuttle, and (4) collection of an electron at the counter electrode by the oxidized redox shuttle after the electron has traversed an external circuit. The design of dye−redox shuttle systems to improve power conversion efficiencies (PCEs) under low light conditions in DSC devices is needed.

Under conditions where the photon flux is low (and, by default, interfacial charge separation events are less frequent), ensuring the rapid regeneration of the neutral dye is critically important. During the regeneration step, the dye and redox shuttle should come into close contact. One approach to improving regeneration is through the noncovalent association of the redox shuttle to the dye via a transient self-assembly process which is known to increase the rate of regenerative electron transfer from the redox shuttle to the oxidized dye.[20−27] Self-assembly approaches that have been recently investigated to improve the rate of dye regeneration include halogen bonding,[21−25] Lewis acid−Lewis base interactions,[26] and alkyl−alkyl van der Waals interactions.[20] In this context, we envision π-stacking between the redox shuttle and the dye could provide a tunable noncovalent interaction that can be harnessed to promote rapid dye regeneration via association of the redox shuttle to the dye and diffusion of the redox shuttle through the electrolyte after dissociation of the oxidized redox shuttle. To the best of our knowledge, π-stacking interactions have not been explicitly studied in DSC devices via rational design of a dye−redox shuttle pair despite the popularity of this approach in other solid−liquid interfacial electron transfer systems such as with electrocatalysis.[28−30]

The donor−π bridge−acceptor (D−π−A) dye design has given rise to some of the highest power-conversion efficiencies (PCEs) observed in organic dye-based DSC devices.[7,31−33] Such dyes are designed to operate by undergoing an

Received: March 4, 2022
Revised: June 6, 2022
Published: June 22, 2022

https://doi.org/10.1021/acs.energyfuels.2c00633
Energy Fuels 2022, 36, 7075−7086

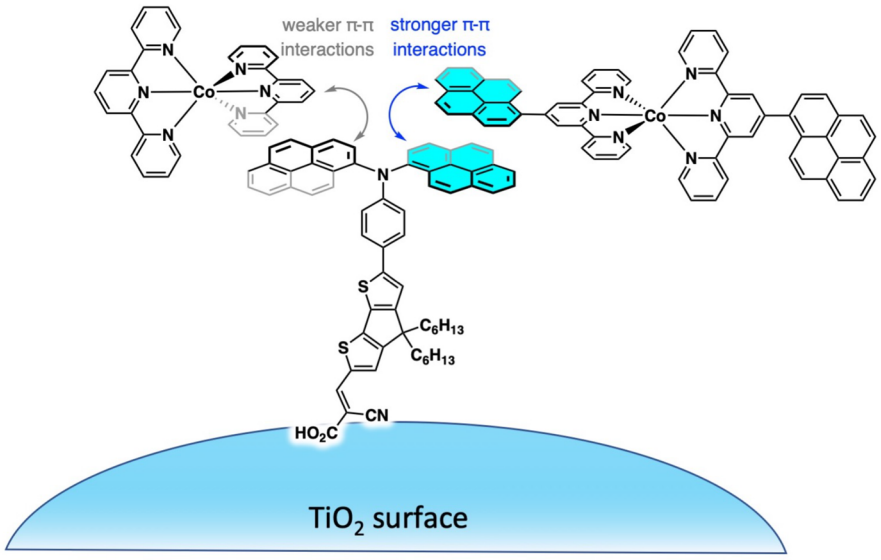

Figure 1. π-Stacking interaction between a TiO_2 bound dye (**SS1**) and $[Co(tpy^{pyr})_2]^{3+/2+}$ (right) compared to $[Co(tpy)_2]^{3+/2+}$ (left).

intramolecular charge transfer (ICT) event upon photoexcitation that separates the electron and hole onto the acceptor and donor regions of the dye, respectively.[34−37] This spatial separation gives rise to extended charge separated state lifetimes upon injection of the electron into TiO_2 when the acceptor is anchored on TiO_2. After an electron is injected into TiO_2, the singly occupied molecular orbital of the dye cation is typically most prevalent on the donor region of the molecule (i.e., the most easily oxidized functionality), which is generally strategically positioned furthest from the TiO_2 surface.

Pyrene is a commonly used building block for the design of π-stacking organic electronic materials[38] which readily undergoes π-stacking unless molecular designs are specifically employed to restrict pyrene−pyrene π-stacking interactions.[38] We envisioned the use of a pyrene-substituted dye with the pyrene groups positioned on the donor region of the dye to facilitate noncovalent interactions between a pyrene substituted redox shuttle and the region of the dye being oxidized upon photoexcitation and electron injection (Figure 1). We reasoned that a pyrene-substituted redox shuttle would introduce desirable π-stacking interactions with the dye to enhance the regenerative electron transfer reaction and improve DSC device PCEs (Figure 1).

Dye **SS1** features two pyrene groups on the triarylamine (TAA) donor, a cyclopentadithiophene (CPDT) π-bridge, and a cyanoacrylic acid acceptor (CAA, Figure 2). The use of two pyrene groups on the TAA was selected for synthetic ease and to provide multiple sites for π-stacking interactions on the dye. An arylamine-based donor on **SS1** was implemented because this type of donor is found in the dyes of the highest performing DSC devices under full sun and low light conditions.[7,31−33,39,40] Likewise, the CPDT π-bridge offers a building block common to many high performance dyes that extends π-conjugation for broader light absorption and features two alkyl chains for increased TiO_2 surface protection to inhibit recombination of electrons in TiO_2 with an oxidized redox shuttle.[4,5,7,8,34−37,41] The CAA acceptor is known to promote facile electron injection into TiO_2.[42]

A 4′-pyrene-2,2′:6′,2″-terpyridine ligated cobalt complex ($[Co(tpy^{pyr})_2]^{3+/2+}$) was prepared as a RS to promote interfacial π-stacking interactions at the dye−TiO_2 interface

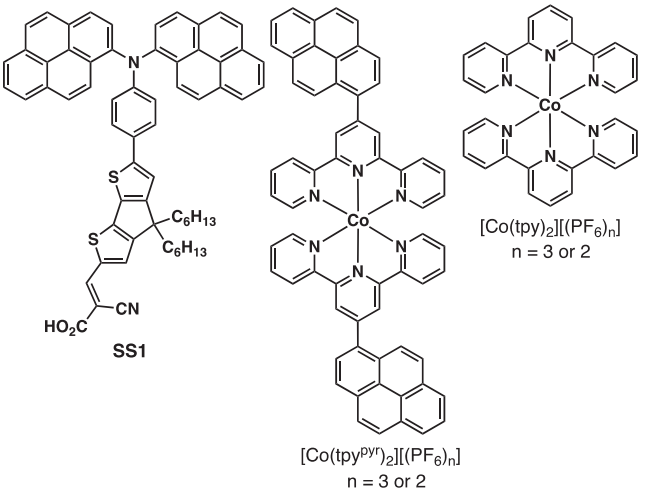

Figure 2. Molecular structures of **SS1**, $[Co(tpy^{pyr})_2][(PF_6)_n]$, and $[Co(tpy)_2][(PF_6)_n]$ where n is 3 or 2.

(Figure 2). Terpyridine ligands on cobalt metal centers were selected because they allow straightforward installation of two pyrene groups in a symmetric complex. More than two pyrene groups were not considered to avoid solubility issues and sluggish mass transport due to the size of the redox shuttle increasing significantly as pyrene groups are added.[43,44] The pyrene groups were installed at the 4′-position of the 2,2′:6′,2″-terpyridine ligand (i.e., on the central pyridine and *para* to the nitrogen atom; Figure 2). As a control, a non-pyrene-substituted cobalt complex ($[Co(tpy)_2]^{3+/2+}$) was also studied, which is anticipated to have weaker π-stacking interactions.

RESULTS AND DISCUSSION

The synthesis of **SS1** began with the bromination of known *N*-phenyl-*N*-(pyren-1-yl)pyren-1-amine (**1**)[45] with *N*-bromosuccinimide to give *N*-(4-bromophenyl)-*N*-(pyren-1-yl)pyren-1-amine (**2**) in 88% yield (Scheme 1). Compound **2** was coupled to known stannylated CPDT (**3**)[46] in 40% yield to give compound **4**. The CPDT group of compound **4** was then formylated via a Vilsmeier−Haack reaction to give **5** in 69%

https://doi.org/10.1021/acs.energyfuels.2c00633
Energy Fuels 2022, 36, 7075−7086

Scheme 1. Synthetic Route to SS1

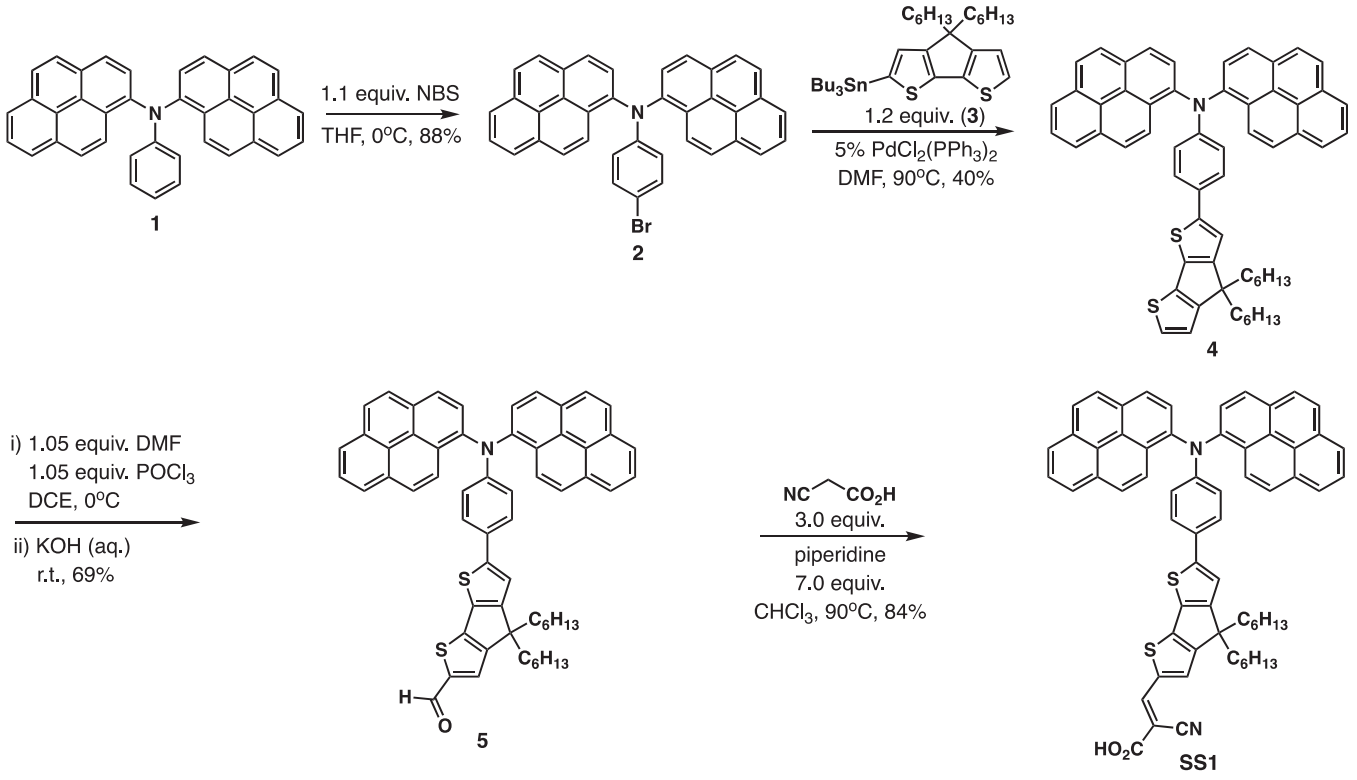

Scheme 2. Synthetic Route to $[Co(tpy^{pyr})_2][(PF_6)_2]$ and $[Co(tpy^{pyr})_2][(PF_6)_3]$

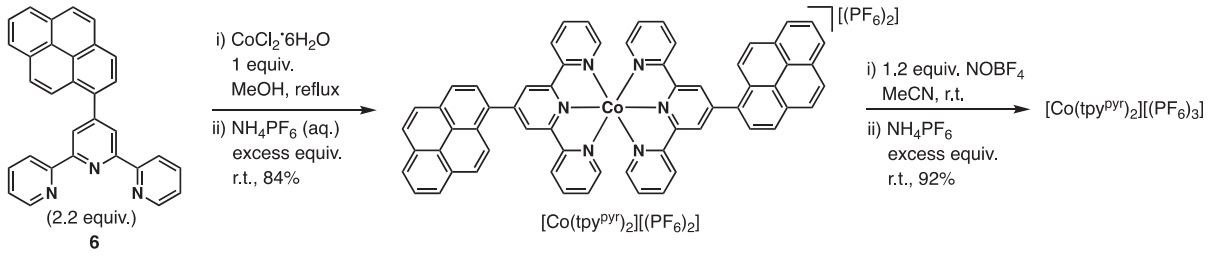

yield. A Knoevenagel reaction with **5** and cyanoacetic acid gave **SS1** in 84% yield. **SS1** was synthesized in four total steps from known compounds in 20% overall yield.

The synthesis of $[Co(tpy^{pyr})_2][(PF_6)_2]$ began with known ligand **6**[47] via a complexation with $CoCl_2{\cdot}6H_2O$ followed by salt metathesis with NH_4PF_6 to give $[Co(tpy^{pyr})_2][(PF_6)_2]$ in 84% yield, similar to reported procedures (Scheme 2).[48] Notably, the perchlorate salt of $[Co(tpy^{pyr})_2]^{2+}$ is known in the literature and has a nearly identical absorption spectrum to that observed in this study.[49] Following a modified synthetic approach,[50] treatment of $[Co(tpy^{pyr})_2][(PF_6)_2]$ with $NOBF_4$ followed by a large excess of NH_4PF_6 led to the formation of $[Co(tpy^{pyr})_2][(PF_6)_3]$ in 92% yield similarly to the literature reported approach. Both complexes without pyrene groups, $[Co(tpy)_2][(PF_6)_2]$ and $[Co(tpy)_2][(PF_6)_3]$, have been previously reported.[51]

The photophysical and electrochemical characteristics of the dye and redox shuttles were investigated to understand the light harvesting capabilities of the DSC devices and the thermodynamic properties that determine the driving forces of electron transfer reactions in the system. The absorption spectrum of **SS1** in dichloromethane (DCM) shows a broad absorbance across the visible region primarily due to a single feature which is assigned as an intramolecular charge transfer (ICT) band (Figure 3). A molar absorptivity of 10500 M^{-1} cm^{-1} is observed with a maximum absorbance (λ_{max}^{abs}) at 521 nm. **SS1** is emissive in DCM with a broad emission from 550 to 850 nm observed with a maximum emission (λ_{max}^{emis} at 656

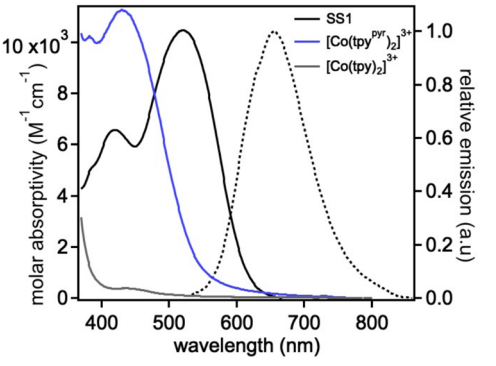

Figure 3. Absorption (solid lines) and emission (dashed line) spectrum of **SS1** in dichloromethane, $[Co(tpy^{pyr})_2][(PF_6)_3]$ in CH_3CN, and $[Co(tpy)_2][(PF_6)_3]$ in CH_3CN at room temperature.

https://doi.org/10.1021/acs.energyfuels.2c00633
Energy Fuels 2022, 36, 7075−7086

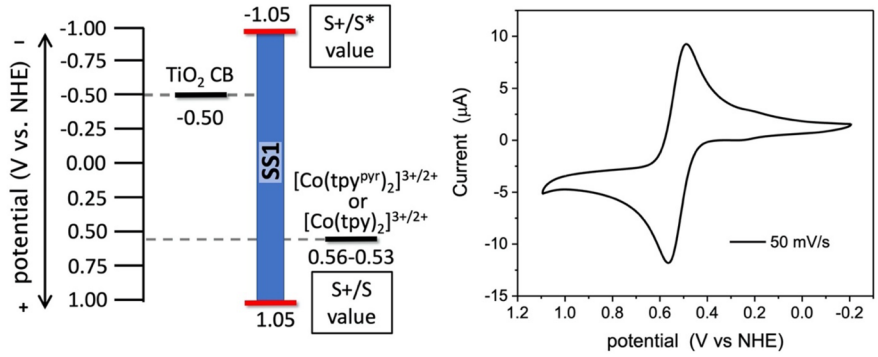

Figure 4. Left: energy level diagram of **SS1**, $[Co(tpy^{pyr})_2]^{3+/2+}$, $[Co(tpy)_2]^{3+/2+}$, and TiO_2 CB. Right: cyclic voltammogram of $[Co(tpy^{pyr})_2]^{3+/2+}$ at 1 mM concentration in CH_3CN with 0.1 M Bu_4NPF_6.

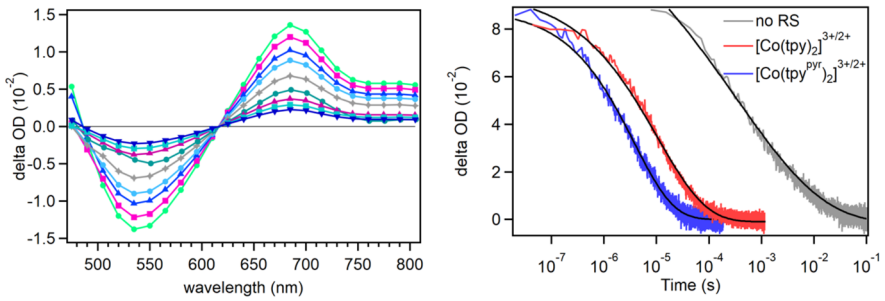

Figure 5. Left: transient absorption spectrum of **SS1**−TiO_2 under an inert electrolyte. Right: transient absorption decay kinetics monitored at 680 nm.

nm. The absorption and emission bands intercept (E_{0-0}) at 591 nm.

The ground-state oxidation potential ($E_{(S+/S)}$) of **SS1** was obtained from cyclic voltammetry (CV) in dichloromethane and found to be 1.05 V versus the normal hydrogen electrode (NHE) (Figure S1). The excited-state oxidation potential ($E_{(S+/S^*)}$) was found to be −1.05 V vs NHE through the equation $E_{(S+/S^*)} = E_{(S+/S)} - E_{(0-0)}$, where the value of $E_{(0-0)}$ in eV was found by taking 1240 nm·eV/$\lambda_{(0-0)}$, which is a common approximation of the equation $E_{(0-0)} = \frac{hc}{\lambda_{(0-0)}}$, where $\lambda_{(0-0)}$ is the intercept of the normalized absorption and emission curves.[52] The conduction band (CB) of TiO_2 is commonly approximated at −0.5 V vs NHE.[42,53−55] This gives a driving force for injection (ΔG_{inj}) of 550 mV, which is sufficient for rapid electron transfer from a photoexcited **SS1** molecule to the TiO_2 CB. CV data collected with $[Co(tpy^{pyr})_2][(PF_6)_2]$ show a potential of 0.53 V vs NHE (Figure 4). The driving force for regeneration (ΔG_{reg}) of the neutral dye with $[Co(tpy^{pyr})_2][(PF_6)_2]$ is found to be 520 mV, which is sufficiently high for a rapid electron transfer reaction to take place. The electrochemical potential of $[Co(tpy)_2][(PF_6)_2]$ is similarly observed to be 0.56 V vs NHE, which indicates minimal influence of the pyrene group on the Co(III/II) redox potentials (Figure S2). Conveniently, this allows for a comparison of the two redox shuttles without a significant variation in ΔG_{reg} (Figure 4). Notably, a faster diffusion coefficient is observed with the $[Co(tpy)_2][(PF_6)_2]$ complex (5.77×10^{-6} cm^2 s^{-1}) compared to the larger $[Co(tpy^{pyr})_2][(PF_6)_2]$ complex (4.37×10^{-6} cm^2 s^{-1}), which could allow for an increase in regeneration rate with $[Co(tpy)_2][(PF_6)_2]$ if the regeneration reaction is diffusion controlled (Figures S3 and S4).

$[Co(tpy^{pyr})_2][PF_6]_2$ was found to absorb photons until ∼600 nm with a λ_{max}^{abs} at 515 nm (and a lower energy shoulder) at a significantly lower molar absorptivity than **SS1** (252 M^{-1} cm^{-1} vs 10500 M^{-1} cm^{-1}; Figure S5). $[Co(tpy^{pyr})_2][PF_6]_3$ has a broad absorption in the visible range from 400 to 550 nm with a λ_{max}^{abs} at 433 nm and a molar absorptivity comparable to **SS1** (11560 M^{-1} cm^{-1} vs 10500 M^{-1} cm^{-1}, respectively; Figure 3). Ideally, the redox shuttle should not absorb light in the region of the spectrum that the dye adsorbs light to achieve maximal performance from a DSC device. However, it is important to note that Co^{2+} is typically present in 5× the concentration of Co^{3+}. For $[Co(tpy^{pyr})_2]$, the Co^{2+} species has a substantially lower molar absorptivity than the Co^{3+} species. Additionally, light entering a DSC device typically arrives at the photoanode first where the dye−TiO_2 is concentrated, and the bulk of the electrolyte containing the light absorbing redox shuttles is above the dye−TiO_2 layer and is only encountered by photons after the dye−TiO_2 layer absorbs available photons first. Thus, exceptional DSC device performances are possible despite redox shuttles absorbing appreciably in the visible spectral range.[56−59] Notably, $[Co(tpy)_2]^{3+/2+}$ absorbs more weakly throughout the visible range relative to $[Co(tpy^{pyr})_2]^{3+/2+}$, which indicates a lower theoretical photocurrent is possible with $[Co(tpy^{pyr})_2]^{3+/2+}$ in DSC devices.

Having found suitable energetics and optical properties for the use of **SS1**, $[Co(tpy^{pyr})_2]^{3+/2+}$, and $[Co(tpy)_2]^{3+/2+}$ in DSC devices, transient absorption spectroscopy (TAS) measurements were undertaken to evaluate the rate of dye regeneration. TAS was performed with **SS1** bound to TiO_2 (**SS1**−TiO_2) to analyze the interfacial charge separated lifetime (eq 3) upon electron injection into TiO_2 (eq 2) from photoexcited **SS1**−TiO_2 (**SS1***−TiO_2; eq 1). For an accurate description of reaction rates, the single wavelength

https://doi.org/10.1021/acs.energyfuels.2c00633
Energy Fuels 2022, 36, 7075−7086

absorbance of the dye cation ($\mathbf{SS1}^+-TiO_2(e^-)$) should be monitored where the oxidized dye predominantly absorbs light with minimal or no contributions from the ground-state dye or redox shuttle. Under an inert electrolyte composed of 0.1 M lithium bis(trifluoromethanesulfonyl)imide (LiTFSI) and 0.5 M 4-*tert*-butylpyridine (TBP), a strong ground-state bleach signal was observed near 535 nm in addition to a signal centered at ~690 nm, which is assigned to $\mathbf{SS1}^+$ (Figure 5). Therefore, absorption changes for $\mathbf{SS1}^+-TiO_2(e^-)$ were monitored at 680 nm where neither the ground state dye nor the redox shuttles absorb appreciably. Given the immediate appearance of the oxidized dye signal, injection (eq 2) was assumed to be completed on a time scale faster than the time resolution of the experiment. The observed kinetic decay data were nonexponential and sufficiently described by a Kohlrausch–Williams–Watt (KWW) stretched exponential decay function via the equation $\Delta OD(t) = \Delta OD_0 \exp[-(t/\tau)^{\beta}]$.[60−63] A mean lifetime value was calculated from the fit using a gamma function distribution of β^{-1} according to the equation $\tau_{KWW} = \tau\beta^{-1}\Gamma(\beta^{-1})$. The $\mathbf{SS1}^+-TiO_2(e^-)$ signal was found to have a lifetime (τ_{KWW}) of 620 μs (or k_{KWW} of 1600 s^{-1} for the back-electron-transfer reaction, eq 3; Table 1).

$$\mathbf{SS1}-TiO_2 + h\nu \rightarrow \mathbf{SS1}^*-TiO_2 \quad (1)$$

$$\mathbf{SS1}^*-TiO_2 \rightarrow \mathbf{SS1}^+-TiO_2(e^-) \quad (2)$$

$$\mathbf{SS1}^+-TiO_2(e^-) \rightarrow \mathbf{SS1}-TiO_2 \quad (3)$$

$$\mathbf{SS1}^+-TiO_2(e^-) + Co^{2+} \rightarrow \mathbf{SS}1-TiO_2(e^-) + Co^{3+} \quad (4)$$

$$\mathbf{SS}1-TiO_2(e^-) + Co^{3+} \rightarrow \mathbf{SS}1-TiO_2 + Co^{2+} \quad (5)$$

Table 1. Fit Parameters Obtained for the $\mathbf{SS1}^+-TiO_2(e^-)$ Signal under Varied Electrolytes

entry	redox shuttle	τ_{KWW} (μs)	k_{KWW} (s^{-1})
1	none	620	1.6×10^3
2	$[Co(tpy^{pyr})_2]^{3+/2+}$	1.5	6.7×10^5
3	$[Co(tpy)_2]^{3+/2+}$	4.2	2.4×10^5

TAS measurements were taken in the presence of 0.25 M Co^{2+}, 0.05 M Co^{3+}, 0.1 M LiTFSI, and 0.5 M TBP to evaluate the electron transfer dynamics under conditions comparable to an operational device. While this electrolyte solution is more complex than simply evaluating the kinetics in the presence of only a redox shuttle, any effect that would be meaningful to DSC device performances must be observable in the presence of the complete electrolyte used in a DSC device. Under these conditions, if the decay rate of $\mathbf{SS1}^+-TiO_2(e^-)$ is significantly faster than the decay rate of $\mathbf{SS1}^+-TiO_2(e^-)$ when using an inert (RS-free) electrolyte, then the decay rate is assumed to be primarily associated with dye regeneration (eq 4). This is a common approach in the DSC literature which may provide a slight overestimation of regeneration efficiency, but it is an approach that is useful for assessing relative regeneration kinetics between two different redox shuttles under complex but similar experimental conditions.[64,65] In the presence of $[Co(tpy^{pyr})_2]^{3+/2+}$, the lifetime of the $\mathbf{SS1}^+-TiO_2(e^-)$ decay decreases dramatically to 1.5 μs (or k_{KWW} of 6.7×10^5 s^{-1}) relative to the inert electrolyte at 620 μs (Figures 5 and S20, Table 1). The lifetime of the $\mathbf{SS1}^+-TiO_2(e^-)$ signal in the presence of $[Co(tpy^{pyr})_2]^{3+/2+}$ is 2.8× shorter than in the presence of $[Co(tpy)_2]^{3+/2+}$ (Figures 5 and S21). This indicates a significant rate increase for dye regeneration (eq 4) in the presence of $[Co(tpy^{pyr})_2]^{3+/2+}$ relative to $[Co(tpy)_2]^{3+/2+}$ (6.7×10^5 s^{-1} vs 2.4×10^5 s^{-1}; Table 1). We note that this data does not conclusively establish a π-stacking interaction between $\mathbf{SS1}-TiO_2$ and $[Co(tpy^{pyr})_2]^{3+/2+}$, but a faster electron transfer event is anticipated if a π-stacking mechanism were taking place between the dye and the redox shuttle as is observed in these studies.

Comparative TAS and DSC device (see below) studies using **SS1**, **A1**, and **Y123** as dyes with $[Co(tpy^{pyr})_2]^{3+/2+}$ were also undertaken (see Figure S19 for dye structures). **A1** is selected as a dye with potentially reduced π-stacking interactions with the redox shuttle by decreasing the aryl group size to benzene on the donor from the pyrene of **SS1**.[66] **Y123** is selected as a high performance dye used frequently in the literature.[1,34] All three dyes have the same π-bridge and acceptor groups. Interestingly, k_{KWW} was found to *increase* with lower pump intensities with **SS1**-sensitized films by using the $[Co(tpy^{pyr})_2]^{3+/2+}$ redox shuttle (Figures S22 and S28). The inverse trend is observed when **A1** and **Y123** are probed under identical conditions (Figures S25, S27, and S28; Table S1). A possible explanation for this observation is that a $\pi-\pi$ stacking interaction is slowing redox shuttle diffusion, leading to slower redox shuttle migration across the film. In this case, a lower pump power would reduce the rate of generation of oxidized dye molecules at TiO_2 and allow for the slow diffusing $[Co(tpy^{pyr})_2]^{2+}$ molecules to become preassociated with the

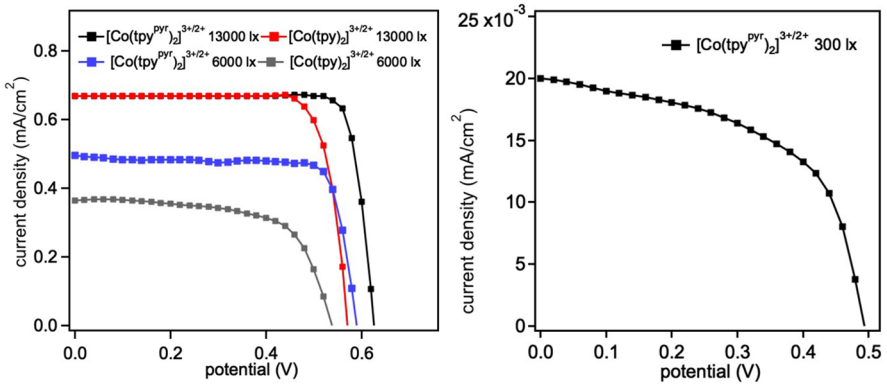

Figure 6. Left: $J-V$ curves of **SS1**-based DSC devices under fluorescent light illumination with circular 0.15 cm^2 active area devices. Right: $J-V$ curve of a **SS1**-based DSC devices under fluorescent illumination (300 lx) with a rectangular 2.8 cm^2 active area device.

https://doi.org/10.1021/acs.energyfuels.2c00633
Energy Fuels 2022, 36, 7075−7086

Table 2. SS1 DSC Device Data[a]

redox shuttle	irradiance (W/m^2)	illuminance (lx)	source	V_{oc} (mV)	J_{sc} (mA/cm^2)	FF (%)	PCE (%)
$[Co(tpy^{pyr})_2]^{3+/2+}$	25	13000	fluorescent	615	0.67	80	13.2
$[Co(tpy)_2]^{3+/2+}$	25	13000	fluorescent	570	0.67	81	12.4
$[Co(tpy^{pyr})_2]^{3+/2+}$	10	6000	fluorescent	590	0.49	79	22.8
$[Co(tpy)_2]^{3+/2+}$	10	6000	fluorescent	540	0.36	64	12.4
$[Co(tpy^{pyr})_2]^{3+/2+}$	–[b]	2300	fluorescent	560	0.18	76	14.2
$[Co(tpy^{pyr})_2]^{3+/2+}$	–[b]	300	fluorescent	490	0.02	55	6.7
$[Co(tpy^{pyr})_2]^{3+/2+}$	1000		AM1.5G	655	5.1	76	2.5
$[Co(tpy)_2]^{3+/2+}$	1000		AM1.5G	638	8.0	69	3.5

[a]The fluorescent light source is an Osram 011318-L 36W/930 tube light. The AM1.5G source is provided via a 300 W Xe lamp with an AM1.5G filtered output with an AAA rating. [b]Power meter accuracy is not high enough to report a value at 300 lx.

dye prior to photoinduced oxidation. To further probe the binding of **SS1** to $[Co(tpy^{pyr})_2]^{2+}$, fluorescence quenching studies were undertaken with varied $[Co(tpy^{pyr})_2]^{2+}$ concentrations (Figures S6–S8). The fluorescence of **SS1** was found to quench as the concentration of $[Co(tpy^{pyr})_2]^{2+}$ increases (Figure S6). The rate of fluorescence quenching was found to be nonlinear versus $[Co(tpy^{pyr})_2]^{2+}$ concentration via a Stern–Volmer plot, which is indicative of a system undergoing association in the ground state prior to photoexcitation (Figure S7). A Hill plot was generated from this data, which shows a binding energy of approximately −5.5 kcal/mol (Figure S8). We hypothesize a moderately favorable binding energy is needed for a π-stacking system to transiently form a $\pi-\pi$ interaction to increase the rate of regeneration. However, the binding energy should be easily overcome with the energy available at room temperature in order for the interaction to be transient, which would allow for the redox shuttle to dissociate from the dye-TiO_2 surface and diffuse to the counter electrode.

To probe the effect of faster regeneration kinetics on device performances, DSC devices were fabricated by using **SS1** dye and each redox shuttle system to better understand the influence of the pyrene group on $[Co(tpy^{pyr})_2]^{3+/2+}$. Because DSC devices have excelled recently in low light applications with record setting performances relative to other solar cell technologies,[7] the performance of **SS1**/$[Co(tpy^{pyr})_2]^{3+/2+}$-based devices were first evaluated under fluorescent lighting by using an Osram 011318-L 36W/930 tube light according to literature precedent.[4] Current density versus voltage curves were collected, and the PCE values were obtained via the equation PCE = $(J_{SC} \times V_{OC} \times FF)/I_0$, where J_{SC} is the short-circuit current density, V_{OC} is the open-circuit voltage, FF is the fill factor, and I_0 is the incident light intensity (Figure 6, Tables 2 and S3). At 13000 lx, **SS1**-based DSC devices with the $[Co(tpy^{pyr})_2]^{3+/2+}$ electrolyte give a PCE value of 13.2%, which compares favorably to devices with a $[Co(tpy)_2]^{3+/2+}$ electrolyte at 12.4% PCE. A significantly higher V_{OC} value is observed with the $[Co(tpy^{pyr})_2]^{3+/2+}$ RS under these conditions. Reducing the illumination intensity by roughly half (6000 lx) further accentuates the differences of these two electrolyte systems with PCE values of 22.8% for $[Co(tpy^{pyr})_2]^{3+/2+}$ and 12.4% for $[Co(tpy)_2]^{3+/2+}$, respectively. Reducing the illumination intensity further to 2300 or 300 lx leads to a diminished PCE with the $[Co(tpy^{pyr})_2]^{3+/2+}$ RS system at 14.2% and 6.7% PCE (Table 2). Notably, the loss in PCE value is very rapid with the $[Co(tpy)_2]^{3+/2+}$ RS as the illumination intensity decreases, resulting in 3.4% PCE at 2300 lx and a low PCE at 300 lx, which was unreliably measurable with our equipment (Table S3). Under full sun irradiation with a solar simulated spectrum (1000 W/m^2), the PCE of $[Co(tpy^{pyr})_2]^{3+/2+}$ remains lower than that of $[Co(tpy)_2]^{3+/2+}$ at 2.5% and 3.5%, respectively (Table 2). Under these conditions, the short-circuit photocurrent density is higher with $[Co(tpy)_2]^{3+/2+}$, but the open circuit voltage and FF are significantly higher with $[Co(tpy^{pyr})_2]^{3+/2+}$. The observed open circuit voltages are discussed in more detail below. The PCE is similar for **SS1** and **Y123** under fluorescent lighting at all light intensities, which shows **SS1** is operating at a high efficiency relative to a well-studied high performing dye (Figures S33 and S34; Tables S4 and S5). However, compared to **A1** (which likely is a more direct comparison of the effects of π-stacking), the efficiency of **SS1** is 32%–238% higher with a higher FF for **SS1** in all cases. The incident photon-to-current conversion efficiency (IPCE) was measured as a function of wavelength for the two systems (Figure S31). A peak IPCE value of 34% is observed with $[Co(tpy^{pyr})_2]^{3+/2+}$-based devices. The higher peak IPCE observed with $[Co(tpy)_2]^{3+/2+}$-based devices (52%) is attributed to the weaker absorbance of $[Co(tpy)_2]^{3+/2+}$ in the visible region. The higher peak IPCE and integrated current agree with the higher photocurrent observed with $[Co(tpy)_2]^{3+/2+}$ under full sun (1000 W/m^2) irradiation.

Interestingly, a literature report suggests that regeneration efficiencies observed under open circuit conditions (such as with typical TAS measurements) are significantly overestimated in many cases and that the regeneration efficiencies at the DSC device maximum power point (MPP) are much lower.[64] TAS measurements at the MPP are significantly more challenging to perform versus open circuit measurements; however, a key outcome of this prior work indicates that a decrease in FF is expected if regeneration at the MPP is problematic. This study also indicates that the loss of FF due to slow MPP regeneration may be exacerbated at lower light intensities. Interestingly, observations in line with faster regeneration at the MPP are observed here with $[Co(tpy^{pyr})_2]^{3+/2+}$ relative to $[Co(tpy)_2]^{3+/2+}$ with fluorescent light (10 W/m^2), solar simulated 10% sun (100 W/m^2), and solar simulated full sun (1000 W/m^2) measurements showing a margin of increase of the FF of 23%, 31%, and 10%, respectively, when the two redox shuttles are compared at these light intensities (Tables 2 and S3, Figures 6 and S32–S33).

The origin of the difference in V_{OC} between the two redox shuttle systems is probed via small modulate photovoltage transient (SMPVT) studies since the two redox shuttles have similar maximum V_{OC} (V_{OC}^{max}) values of 1.06–1.03 V according to the equation $V_{OC}^{max} = E_{Co^{3+}/Co^{2+}} - TiO_2$ CB potential. This indicates a significantly larger open circuit voltage loss (V_{OC}^{loss}) at 6000 lx for the $[Co(tpy)_2]^{3+/2+}$-based electrolyte compared to the $[Co(tpy^{pyr})_2]^{3+/2+}$-based electrolyte (520 mV vs 440 mV)

https://doi.org/10.1021/acs.energyfuels.2c00633
Energy Fuels 2022, 36, 7075–7086

according to the equation $V_{OC}^{loss} = V_{OC}^{max} - V_{OC}^{obs}$, where V_{OC}^{obs} is the observed V_{OC} of the DSC device.[67] SMPVT measurements allow for an observation of electron lifetimes in TiO_2 under irradiation via small changes to the light intensity.[68,69] SMPVT measurements reveal a modestly longer electron lifetime in TiO_2 when the $[Co(tpy^{pyr})_2]^{3+/2+}$-based electrolyte is used (Figure 7). This observation suggests that recombination of

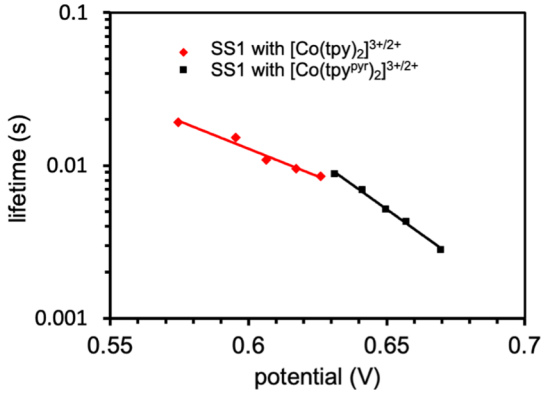

Figure 7. Small modulated photovoltage transient measurements.

electrons in TiO_2 with Co^{3+} (eq 5) is slower with the $[Co(tpy^{pyr})_2]^{3+/2+}$ RS. This is consistent with the higher open circuit voltage obtained with $[Co(tpy^{pyr})_2]^{3+/2+}$-based DSC devices. Plausible explanations for the slower recombination rates include (1) less diffusion of the oxidized RS past the dye to the TiO_2 surface due to the increased size of the $[Co(tpy^{pyr})_2]$ redox shuttle and (2) a favorable π-stacking interaction between the dye and the redox shuttle that slows diffusion of the oxidized RS past the dye to the TiO_2 surface, thus diminishing the rate of recombination. It is observed in the literature that dye−redox shuttle association can lead to slower rates of recombination presumably due to the dye orientation at the surface holding the oxidized redox shuttle (formed after dye regeneration) away from the TiO_2 surface.[50,70]

Current dynamic measurements at varied light intensities were conducted because two diffusion-related arguments are postulated to explain the slower recombination of electrons in TiO_2 with the $[Co(tpy^{pyr})_2]^{3+/2+}$-based electrolyte (Figure 8). The plots in Figure 8 show the behavior associated with the irradiation being shuttered on/off with the two redox shuttle systems at five different light intensities by using a solar simulated spectrum. The $[Co(tpy^{pyr})_2]^{3+/2+}$-based device shows a large spike at full sun intensity (1000 W/m^2) before reaching near-steady-state photocurrent production. This large spike is indicative of slow diffusion of the redox shuttle in the device with the initial concentration of Co^{2+} being high near the dye (the spike) and then quickly dissipating to a lower steady-state concentration of Co^{2+} as the redox shuttle continues to regenerate the dye at the TiO_2 surface but diffuses slowly.[71] As the light intensity is decreased, the magnitude of this initial spike is decreased and eventually not observed at 10% sun (100 W/m^2) intensity. Additionally, the current from the devices is generated more efficiently at lower sun intensities which is represented by the dashed lines that show the extrapolated current generated if the same efficiency at a given irradiation intensity were observed at 1 sun. The dashed lines show more efficient current generation from lower light intensities after a steady state is reached. The extrapolated current analysis also suggests diffusion is problematic because in cases where the photon flux is lowered, the slow diffusion of $[Co(tpy^{pyr})_2]^{3+/2+}$ becomes competitive with Co^{2+} depletion at the dye−electrolyte interface. In contrast, the $[Co(tpy)_2]^{3+/2+}$-based devices show no spike in current as the light is shuttered on. The extrapolated current values show similar current generation efficiencies at the steady state for each of the irradiation intensities. It is not obvious if the diffusion limitations are only due to redox shuttle size or if the presence of a π-stacking interaction is resulting in slower diffusion. However, these results are consistent with a π-stacking expanation, which is also suggested by the FF observations described above at varied irradiation intensities.

CONCLUSION

A dye featuring two pyrene substituents at the donor position was synthesized and evaluated in a DSC environment by using a pyrene-substituted redox shuttle and an unsubstituted analogue for comparison. The optical and electronic properties of the dye and the two redox shuttles were measured by using absorption spectroscopy and cyclic voltammetry. The data show a favorable electron transfer reaction during dye

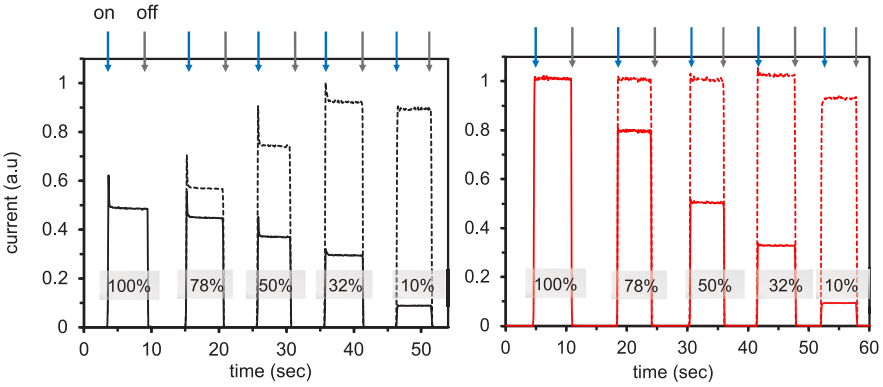

Figure 8. Current dynamics plots for **SS1**-based DSC devices with $[Co(tpy^{pyr})_2]^{3+/2+}$ (left, black) and $[Co(tpy)_2]^{3+/2+}$ (right, red). The solid lines are the observed values, and the dashed lines are normalized extrapolated currents found by dividing the observed values by the light intensity used (listed as percentage of full sun intensity on the graph). The blue arrows indicate where the source is shuttered on, and the gray arrows indicate where the source is shuttered off.

https://doi.org/10.1021/acs.energyfuels.2c00633
Energy Fuels 2022, 36, 7075−7086

regeneration. TAS measurements show a 2.8× faster electron transfer reaction between the oxidized dye and the $[Co(tpy^{pyr})_2]^{2+}$ redox shuttle compared to the $[Co(tpy)_2]^{2+}$ redox shuttle potentially due to the former having a stronger π-stacking interaction with the dye. DSC devices were fabricated, and device performance was evaluated under low light conditions. Results show that significantly higher PCE values are obtained with $[Co(tpy^{pyr})_2]^{3+/2+}$-based devices relative to $[Co(tpy)_2]^{3+/2+}$-based devices (22.8% vs 12.4%, respectively). Under full sun irradiation, the PCE decreased in both systems but was higher with $[Co(tpy)_2]^{3+/2+}$- rather than $[Co(tpy^{pyr})_2]^{3+/2+}$-based devises (3.5% vs 2.5%, respectively). Higher V_{OC} values and longer charge separated lifetimes were observed in the $[Co(tpy^{pyr})_2]^{3+/2+}$-based DSC devices due to slower recombination rates relative to the $[Co(tpy)_2]^{3+/2+}$-based devices. This suggests a favorable π-stacking interaction between the dye and the $[Co(tpy^{pyr})_2]^{3+/2+}$−redox shuttle may be present. Furthermore, slow regeneration in the $[Co(tpy)_2]^{3+/2+}$-based devices accounts for the decrease in the measured fill factor. Current dynamic data show that the $[Co(tpy^{pyr})_2]^{3+/2+}$-based devices have a diffusion limitation under full sun irradiation, which explains the decreased device performance under these conditions. However, because diffusion limitation is not apparent under low light conditions, better device performance was observed with the $[Co(tpy^{pyr})_2]^{3+/2+}$ redox shuttle. Future studies will focus on designing a pyrene-based donor dye with a broad absorption spectrum covering the fluorescent light spectrum. Additionally, these studies suggest design rules governing traditional full sun irradiation high performance redox shuttles (e.g., reduce redox shuttle size for fast diffusion) are not as important as rapid regeneration under low light intensity conditions.

EXPERIMENTAL SECTION

General Information. All commercially obtained reagents were used as received. All synthetic reactions were performed under a nitrogen atmosphere. Thin-layer chromatography (TLC) was conducted with Sorbent Technologies, Inc., Silica XHL TLC plates and visualized with a 254 nm UV lamp. Column chromatography was performed by using Sorbent Technologies, Inc., silica gel, porosity 60 Å, 40−63 μm (230 × 400 mesh), via flash column chromatography with a CombiFlash Rf+ system. ^{1}H NMR spectra were recorded on a Bruker Avance 400 (400 MHz) spectrometer, reported in ppm, and referenced to the residual protiated solvent as $CHCl_3$ at 7.26 ppm and DMSO at 2.50 ppm. Peaks are reported as s = singlet, d = doublet, t = triplet, and m = multiplet; coupling constant (hertz); integration). Absorbance spectra were measured with a Cary 5000 UV−vis−NIR spectrometer. Cyclic voltammograms were measured with a CH Instruments electrochemical analyzer (Model CHI602E). CV measurements were performed by using a platinum counter electrode, an Ag wire quasi-reference electrode, and a glassy carbon working electrode. Cyclic voltammograms were collected with a scan rate of 100 mV/s in dichloromethane (DCM) or acetonitrile solutions containing 0.1 M Bu_4NPF_6 as the supporting electrolyte unless otherwise noted. Ferrocene was used as the reference standard and taken as 0.70 V versus normal hydrogen electrode (NHE) in DCM and 0.64 V versus NHE in CH_3CN.[72,73] FT-IR experiments were recorded on a Bruker Alpha FT-IR spectrometer. Electrospray ionization (ESI) high-resolution mass spectrometry (HRMS) data were collected with a Waters Synapt XS instrument.

***N*-(4-Bromophenyl)-*N*-(pyren-1-yl)pyren-1-amine (2).** To a flame-dried, N_2-filled round-bottom flask was added *N*-phenyl-*N*-(pyren-1-yl)pyren-1-amine (**1**)[45] (0.135 g, 0.27 mmol) and anhydrous tetrahydrofuran (THF) (1.5 mL). The mixture was cooled to 0 °C and freshly recrystallized *N*-bromosuccinimide (0.053 g, 0.30 mmol) was added. After 4 h, the product was extracted with DCM and $NaHCO_3$(aq). After separating and drying the organic layer with Na_2SO_4, the volatiles were removed by a rotary evaporator, and the crude mixture was purified by silica gel flash chromatography using a mobile phase of hexane:DCM (50:50). After evaporation of the solvent, the product (**2**) was obtained in 88% yield (0.137 g, 0.239 mmol) as a green solid. ^{1}H NMR (400 MHz, $CDCl_3$): δ 8.30 (d, J = 9.2 Hz, 2H), 8.20 (d, J = 8.8 Hz, 2H), 8.14 (d, J = 7.8 Hz, 2H), 8.10−7.95 (m, 10H), 7.81 (d, J = 8.2 Hz, 2H), 7.23 (d, J = 9.0 Hz, 2H), 6.67 (d, J = 6.8 Hz, 2H). IR (neat, cm $^{-1}$): 3055, 2991, 2305, 1419, 1274, 895. HRMS ESI (positive mode) m/z calcd for $C_{38}H_{22}BrN$ $[M]^+$: 571.0936; found 571.0949.

***N*-(4-(4,4-Dihexyl-4*H*-cyclopenta[2,1-*b*:3,4-*b*′]dithiophen-2-yl)phenyl)-*N*-(pyren-1-yl)pyren-1-amine (4).** To a pressure flask was added tributyl(4,4-dihexyl-4*H*-cyclopenta[2,1-*b*:3,4-*b*′]-dithiophen-2-yl)stannane (**3**)[46] (0.340 g, 0.534 mmol), *N*-(4-bromophenyl)-*N*-(pyren-1-yl)pyren-1-amine (**2**) (0.255 g, 0.445 mmol), and *N*,*N*-dimethylformamide (DMF, 1.78 mL). Next, $PdCl_2(PPh_3)_2$ (0.016 g, 0.022 mmol) was added, the flask was sealed, and the reaction mixture was stirred at 90 °C overnight. The reaction mixture was extracted with DCM:hexanes (1:1) and water. The organic layer was dried with Na_2SO_4. The volatile components were removed via rotary evaporator, and the oil was left under vacuum overnight. The crude mixture was then purified by flash chromatography with a silica column and DCM:hexanes (20:80) as eluent. After evaporation of the solvent, the product (**4**) was obtained in 40% yield (0.146 g, 0.174 mmol) as a yellow solid. Note: there are unknown impurities in the ^{1}H NMR spectrum at ∼5% the area of nearby peaks. These impurities were not readily removed during purification attempts; however, after carrying forward this mixture into the next reaction, the impurities could be removed. ^{1}H NMR (400 MHz, $CDCl_3$): δ 8.36 (d, J = 9.2 Hz, 2H), 8.20 (d, J = 7.6 Hz, 2H), 8.15−7.90 (m, 12H), 7.83 (d, J = 8.2 Hz, 2H), 7.41 (d, J = 8.8 Hz, 2H), 7.13 (d, J = 4.8 Hz, 1H), 7.05 (s, 1H), 6.91 (d, J = 4.8 Hz, 1H), 6.82 (d, J = 8.8 Hz, 2H), 1.83−1.79 (m, 4H), 1.18−1.12 (m, 12H), 0.98−0.89 (m, 4H), 0.82−0.78 (m, 6H). IR (neat, cm^{-1}): 2993, 2885, 1595, 1486, 1261, 1150. HRMS ESI (positive mode) m/z calcd for $C_{59}H_{51}NS_2$ $[M]^+$: 837.3463; found 837.3424.

6-(4-(Di(pyren-1-yl)amino)phenyl)-4,4-dihexyl-4*H*-cyclopenta[2,1-*b*:3,4-*b*′]dithiophene-2-carbaldehyde (5). To a round-bottom flask was added *N*-(4-(4,4-dihexyl-4*H*-cyclopenta[2,1-*b*:3,4-*b*′]dithiophen-2-yl)phenyl)-*N*-(pyren-1-yl)pyren-1-amine (**4**) (0.046 g, 0.055 mmol), DMF (16.2 μL, 0.174 mmol), and dichloroethane (DCE, 0.14 mL). The mixture was degassed with N_2 and cooled to 0 °C. $POCl_3$ (5.4 μL, 0.058 mmol) was then added. After 8 h, KOH(aq) and DCM were added. The reaction was shaken vigorously. The organics were separated and dried with Na_2SO_4, and the volatiles were evaporated. The product was purified by silica gel flash chromatography using a hexanes:ethyl acetate (95:5) eluent. After evaporation of the solvent, the product (**5**) was obtained in 69% yield (0.033 g, 0.038 mmol) as an orange solid. ^{1}H NMR (400 MHz, $CDCl_3$): δ 9.80 (s,1H), 8.35 (d, J = 9.2 Hz, 2H), 8.21 (d, J = 7.6 Hz, 2H), 8.15−7.90 (m, 12H), 7.85 (d, J = 8.2 Hz, 2H), 7.52 (s, 1H), 7.42 (d, J = 6.7 Hz, 2H), 7.06 (s, 1H), 6.81 (d, J = 8.7 Hz, 2H), 1.90−1.78 (m, 4H), 1.18−1.13 (m, 12H), 0.97−0.88 (m, 4H), 0.82−0.78 (m, 6H). IR (neat, cm^{-1}): 2951, 2927, 2854, 1635, 1588, 1486, 1434, 1330, 1261, 1181. HRMS ESI (positive mode) m/z calcd for $C_{60}H_{51}NOS_2$ $[M]^+$: 865.3412; found 865.3400.

(*E*)-2-Cyano-3-(6-(4-(di(pyren-1-yl)amino)phenyl)-4,4-dihexyl-4*H*-cyclopenta[2,1-*b*:3,4-*b*′]dithiophen-2-yl)acrylic Acid (SS1). To a round-bottom flask was added 6-(4-(di(pyren-1-yl)amino)phenyl)-4,4-dihexyl-4*H*-cyclopenta[2,1-*b*:3,4-*b*′]-dithiophene-2-carbaldehyde (**5**) (0.033 mg, 0.038 mmol) and $CHCl_3$ (0.063 mL). The mixture was degassed with N_2. Then, piperidine (0.023 g, 0.266 mmol) and cyanoacetic acid (0.0097 g, 0.114 mmol) were added. The flask was sealed, and the reaction mixture was heated at 90 °C. After 4 h, the reaction mixture was extracted with DCM and water. The organics were dried with Na_2SO_4, and the volatiles were removed via rotary evaporator. The mixture was kept under vacuum overnight. The product was purified via silica gel flash chromatography with DCM:methanol (95:5) as eluent. After evaporation of the

https://doi.org/10.1021/acs.energyfuels.2c00633
Energy Fuels 2022, 36, 7075−7086

solvent, the product (**SS1**) was obtained in 73% yield (0.026 mg, 0.027 mmol) as a deep red solid. ^{1}H NMR (400 MHz, $CDCl_3$): δ 8.34 (d, J = 9.2 Hz, 2H), 8.25 (s, 1H), 8.21 (d, J = 7.8 Hz, 2H), 8.15−7.96 (m, 12H), 7.86 (d, J = 8.2 Hz, 2H), 7.58 (br s, 1H), 7.42 (d, J = 8.8 Hz, 2H), 7.06 (s, 1H), 6.80 (d, J = 8.6 Hz, 2H), 1.88−1.82 (m, 4H), 1.21−1.10 (m, 12H), 0.93−0.87 (m, 4H), 0.81−0.78 (m, 6H). IR (neat, cm^{-1}): 3400 (broad band), 2900, 2850, 1700, 1650, 1450, 1350, 1250. HRMS ESI (negative mode) m/z calcd for $C_{63}H_{51}N_2O_2S_2$ $[M - H]^-$: 931.3392; found 931.3324.

[Co(tpy^{pyr})$_2$][(PF$_6$)$_2$]. To a solution of $CoCl_2{\cdot}6H_2O$ (0.347 g, 1.46 mmol) in degassed methanol was added 4′-(pyren-1-yl)-2,2′:6′,2″-terpyridine (**6**) (1.4 g, 3.22 mmol) as a solid. The solution was refluxed for 4 h under N_2 and cooled to room temperature. The solvent was removed with a rotary evaporator, and a concentrated aqueous solution of ammonium hexafluorophosphate (8.0 equiv) was added. The resulting precipitate was filtered and washed with water and then Et_2O to remove water. The precipitate was collected and dried under vacuum. Yield = 84% (1.5 g). ^{1}H NMR ($(CD_3)_2CO$, 400 MHz): δ 95.78 (br s, 2H), 55.64 (s, 4H), 43.74 (s, 4H), 33.48 (s, 4H), 13.61 (d, 4H), 9.97 (dd, 4H), 9.35 (m, 12H), 8.69 (s, 4H). Elemental Analysis Calcd for $C_{62}H_{38}CoF_{12}N_6P_2$ (1215.89 g/mol): C, 61.25; H, 3.15; N, 6.91. Found: C, 60.95; H, 3.32; N, 6.71%. HR-MS m/z calcd for $C_{62}H_{38}CoF_{12}N_6P_2$ $[M]^+$, 1215.18; found, 1215.16. UV−vis: λ_{abs} 515 nm (ε = 252 M^{-1} cm^{-1}) in acetonitrile. $E_{1/2}$ value = 0.53 V versus NHE in acetonitrile.

[Co(tpy^{pyr})$_2$][(PF$_6$)$_3$]. A small excess of $NOBF_4$ (1.2 equiv, 0.040 g, 0.344 mmol) was added to a 10 mL solution of $[Co(tpy^{pyr})_2][(PF_6)_2]$ (0.35 g, 0.287 mmol) in acetonitrile. The solvent was then reduced by rotary evaporator to 2 mL, and a large excess of NH_4PF_6 was added to the solution with the addition of 8 mL of acetonitrile. The final product was precipitated by adding diethyl ether and filtered. Yield = 92% (0.36 g). ^{1}H NMR ($(CD_3)_2CO$, 300 MHz): δ 9.81 (s, 4H), 9.49 (d, 4H), 8.85 (d, 2H), 8.68 (s, 4H), 8.53−8.42 (m, 12H), 8.28−8.20 (m, 8H), 7.72 (t, 4H). ^{13}C{^{1}H} NMR (400 MHz, CD_3CN): δ = 159.7, 157.3, 157.0, 153.8, 144.2, 134.3, 134.2, 132.4, 132.0, 131.8, 131.8, 130.7, 130.7, 130.1, 129.6, 129.2, 128.3, 128.2, 1287.8, 127.3, 126.4, 125.7, 125.2, 124.8. HR-MS m/z calcd for $[M]^+$ 1360.14; found: 1360.12. UV−vis: λ_{abs} 433 nm (ε = 11560 M^{-1} cm^{-1}) in acetonitrile.

DSC Device Fabrication. Working electrodes were fabricated according to a previously reported literature procedure[74] and sensitized by immersion in a 0.3 mM **SS1** dye solution in THF:EtOH (1:4) for 16 h at room temperature. PEDOT counter electrodes were fabricated according to a literature procedure[75] and used for all DSC devices. For devices analyzed at light intensities >300 lx, the active area is circular behind a black mask with an illumination area of 0.15 cm^2. For devices analyzed at light intensities of 300 lx, the active area is rectangular behind a black mask with an illumination area of 2.8 cm^2 as has been previously used in the literature to increase the absolute amount of current measured for improved accuracy with our instruments.[7]

DSC Device Characterization. DSC devices under solar simulated conditions were characterized according to a previously reported literature procedure[74] using current density−voltage (J−V), incident photon to current conversion efficiency (IPCE), small modulated photovoltage transient (SMPVT), and current dynamic measurements. Fluorescent light measurements were conducted under varied light intensities by changing the irradiation distance using an OSRAM 930 warm-white, fluorescent light source (bulb 011318), and irradiation intensities were measured and calibrated by using an Amprobe SOLAR-100 m (for W/m^2 measurements) and a Dr. Meter LX1330B (for lux measurements). Current density−voltage measurements under fluorescent lighting used a Keithley 2400 source meter and SweepMe! software (ver. 1.5.5) taking data points every 20 mV with ∼15 s equilibration time allowed between each data point collected. The potential range scanned was determined for each device by first measuring the device voltage with a Fluke 87 V Max multimeter. Scans in the forward and reverse directions overlay without any signs of hysteresis at this scan rate.

TAS Sample Preparation. TAS films (3 μm thickness) were fabricated according to a previously reported literature procedure.[50] TAS films were immersed in 0.3 mM **SS1** dye solution in THF:EtOH (1:4) for 16 h. The films and electrolyte were sealed with a glass coverslip in place of the typical counter electrode position.

Transient Absorption Spectroscopy. Time-resolved absorption measurements were performed with an Edinburgh LP980 optical system (Edinburgh Instruments, UK). Excitation at 532 nm was provided by a Continuum Surelite pulsed Nd:YAG laser (Amplitude) equipped with a frequency-doubling crystal. The initial laser intensity was set to ∼500 μJ cm^{-2} and adjusted to ∼250 and 25 μJ cm^{-2} by using reflective neutral density filters (ThorLabs) and a plano-concave lens to expand the beam for lower laser intensity measurements. The probe source was a 150 W xenon arc lamp run in CW mode to reduce the probe photon flux. The probe was passed through filters to block <400 nm before the sample and detected with a fast photomultiplier tube and recorded by a digital oscilloscope. Sample devices were positioned at a 45° angle relative to the pump and probe sources. Kinetic traces used to estimate the kinetics of the dye−TiO_2 decay were averaged over 3000 consecutive laser shots to achieve a high signal-to-noise ratio.

■ ASSOCIATED CONTENT

Supporting Information

The Supporting Information is available free of charge at https://pubs.acs.org/doi/10.1021/acs.energyfuels.2c00633.

Cyclic voltammograms, steady-state absorption spectra, ^{1}H and ^{13}C NMR spectra, transient absorption spectroscopy data, and DSC device data (PDF)

■ AUTHOR INFORMATION

Corresponding Authors

Nathan I. Hammer − *Department of Chemistry and Biochemistry, 322 Coulter Hall, University of Mississippi, University, Mississippi 38677, United States;* orcid.org/0000-0002-6221-2709; Email: nhammer@olemiss.edu

Jonah W. Jurss − *Department of Chemistry and Biochemistry, 322 Coulter Hall, University of Mississippi, University, Mississippi 38677, United States;* orcid.org/0000-0002-2780-3415; Email: jwjurss@olemiss.edu

Jared H. Delcamp − *Department of Chemistry and Biochemistry, 322 Coulter Hall, University of Mississippi, University, Mississippi 38677, United States;* orcid.org/0000-0001-5313-4078; Email: delcamp@olemiss.edu

Authors

Dinesh Nugegoda − *Department of Chemistry and Biochemistry, 322 Coulter Hall, University of Mississippi, University, Mississippi 38677, United States;* orcid.org/0000-0002-5456-8940

Shrabanti Bhattacharya − *Department of Chemistry and Biochemistry, 322 Coulter Hall, University of Mississippi, University, Mississippi 38677, United States*

Leigh Anna Hunt − *Department of Chemistry and Biochemistry, 322 Coulter Hall, University of Mississippi, University, Mississippi 38677, United States;* orcid.org/0000-0002-7681-3599

Samantha J. Schwartz − *Department of Chemistry and Biochemistry, 322 Coulter Hall, University of Mississippi, University, Mississippi 38677, United States*

Zane H. Turner − *Department of Chemistry and Biochemistry, 322 Coulter Hall, University of Mississippi, University, Mississippi 38677, United States*

Complete contact information is available at:

https://pubs.acs.org/10.1021/acs.energyfuels.2c00633

Notes

The authors declare no competing financial interest.

■ ACKNOWLEDGMENTS

The authors thank the National Science Foundation (NSF) for supporting this research via NSF Award 1757220. S.J.S., N.I.H., and J.H.D. thank the NSF for support via REU Award 1757888.

■ REFERENCES

(1) Munoz-Garcia, A. B.; Benesperi, I.; Boschloo, G.; Concepcion, J. J.; Delcamp, J. H.; Gibson, E. A.; Meyer, G. J.; Pavone, M.; Pettersson, H.; Hagfeldt, A.; Freitag, M. Dye-sensitized solar cells strike back. *Chem. Soc. Rev.* **2021**, *50*, 12450−12550.

(2) Nam, S.-H.; Lee, K. H.; Yu, J.-H.; Boo, J.-H. Review of the Development of Dyes for Dye-Sensitized Solar Cells. *Appl. Sci. Converg. Technol.* **2019**, *28*, 194−206.

(3) Polman, A.; Knight, M.; Garnett, E. C.; Ehrler, B.; Sinke, W. C. Photovoltaic materials: Present efficiencies and future challenges. *Science* **2016**, *352*, aad4424.

(4) Freitag, M.; Teuscher, J.; Saygili, Y.; Zhang, X.; Giordano, F.; Liska, P.; Hua, J.; Zakeeruddin, S. M.; Moser, J.-E.; Grätzel, M.; Hagfeldt, A. Dye-sensitized solar cells for efficient power generation under ambient lighting. *Nat. Photonics* **2017**, *11*, 372−378.

(5) Cao, Y.; Liu, Y.; Zakeeruddin, S. M.; Hagfeldt, A.; Grätzel, M. Direct Contact of Selective Charge Extraction Layers Enables High-Efficiency Molecular Photovoltaics. *Joule* **2018**, *2*, 1108−1117.

(6) Haridas, R.; Velore, J.; Pradhan, S. C.; Vindhyasarumi, A.; Yoosaf, K.; Soman, S.; Unni, K. N. N.; Ajayaghosh, A. Indoor Light Harvesting Dye-sensitized Solar Cells Surpassing 30% Efficiency without Co-sensitizers. *Mater. Adv.* **2021**, *2*, 7773−7787.

(7) Zhang, D.; Stojanovic, M.; Ren, Y.; Cao, Y.; Eickemeyer, F. T.; Socie, E.; Vlachopoulos, N.; Moser, J. E.; Zakeeruddin, S. M.; Hagfeldt, A.; Gratzel, M. A molecular photosensitizer achieves a Voc of 1.24 V enabling highly efficient and stable dye-sensitized solar cells with copper(II/I)-based electrolyte. *Nat. Commun.* **2021**, *12*, 1777.

(8) Michaels, H.; Rinderle, M.; Freitag, R.; Benesperi, I.; Edvinsson, T.; Socher, R.; Gagliardi, A.; Freitag, M. Dye-sensitized solar cells under ambient light powering machine learning: towards autonomous smart sensors for the internet of things. *Chem. Sci.* **2020**, *11*, 2895−2906.

(9) Khamrang, T.; Velusamy, M.; Ramesh, M.; Jhonsi, M. A.; Jaccob, M.; Ramasubramanian, K.; Kathiravan, A. IoT-enabled dye-sensitized solar cells: an effective embedded tool for monitoring the outdoor device performance. *RSC Adv.* **2020**, *10*, 35787−35791.

(10) Aslam, A.; Mehmood, U.; Arshad, M. H.; Ishfaq, A.; Zaheer, J.; Ul Haq Khan, A.; Sufyan, M. Dye-sensitized solar cells (DSSCs) as a potential photovoltaic technology for the self-powered internet of things (IoTs) applications. *Sol. Energy* **2020**, *207*, 874−892.

(11) Li, W.; Pu, Y.; Ge, B.; Wang, Y.; Yu, D.; Qin, S. Dye-sensitized solar cells based on natural and artificial phycobiliproteins to capture low light underwater. *Int. J. Hydrog. Energy* **2019**, *44*, 1182−1191.

(12) Saifullah, M.; Gwak, J.; Yun, J. H. Comprehensive review on material requirements, present status, and future prospects for building-integrated semitransparent photovoltaics (BISTPV). *J. Mater. Chem. A* **2016**, *4*, 8512−8540.

(13) Biyik, E.; Araz, M.; Hepbasli, A.; Shahrestani, M.; Yao, R.; Shao, L.; Essah, E.; Oliveira, A. C.; del Caño, T.; Rico, E.; Lechón, J. L.; Andrade, L.; Mendes, A.; Atlı, Y. B. A key review of building integrated photovoltaic (BIPV) systems. *Eng. Sci. Technol.* **2017**, *20*, 833−858.

(14) Roy, A.; Ghosh, A.; Bhandari, S.; Selvaraj, P.; Sundaram, S.; Mallick, T. K. Color Comfort Evaluation of Dye-Sensitized Solar Cell (DSSC) Based Building-Integrated Photovoltaic (BIPV) Glazing after 2 Years of Ambient Exposure. *J. Phys. Chem. C* **2019**, *123*, 23834−23837.

(15) Kinoshita, T.; Nonomura, K.; Joong Jeon, N.; Giordano, F.; Abate, A.; Uchida, S.; Kubo, T.; Seok, S. I.; Nazeeruddin, M. K.; Hagfeldt, A.; Grätzel, M.; Segawa, H. Spectral splitting photovoltaics using perovskite and wideband dye-sensitized solar cells. *Nat. Commun.* **2015**, *6*, 8834.

(16) Sherman, B. D.; Sheridan, M. V.; Wee, K.-R.; Marquard, S. L.; Wang, D.; Alibabaei, L.; Ashford, D. L.; Meyer, T. J. A Dye-Sensitized Photoelectrochemical Tandem Cell for Light Driven Hydrogen Production from Water. *J. Am. Chem. Soc.* **2016**, *138*, 16745−16753.

(17) Cheema, H.; Rodrigues, R. R.; Delcamp, J. H. Sequential series multijunction dye-sensitized solar cells (SSM-DSCs): 4.7 V from a single illuminated area. *Energy Environ. Sci.* **2017**, *10*, 1764−1769.

(18) Cheema, H.; Delcamp, J. H. The Role of Antireflective Coating CYTOP, Immersion Oil, and Sensitizer Selection in Fabricating a 2.3 V, 10% Power Conversion Efficiency SSM-DSC Device. *Adv. Energy Mater.* **2019**, *9*, 1900162.

(19) Cheema, H.; Watson, J.; Delcamp, J. H. Integrating GaAs, Si, and Dye-Sensitized Solar Cells in Multijunction Devices and Probing Harsh Condition Behavior. *ACS Appl. Electron. Mater.* **2021**, *3*, 316−324.

(20) Cho, I.; Wagner, P.; Innis, P. C.; Mori, S.; Mozer, A. J. Substrate-Dependent Electron-Transfer Rate of Mixed-Ligand Electrolytes: Tuning Electron-Transfer Rate without Changing Driving Force. *J. Am. Chem. Soc.* **2021**, *143*, 488−495.

(21) Parlane, F. G. L.; Mustoe, C.; Kellett, C. W.; Simon, S. J.; Swords, W. B.; Meyer, G. J.; Kennepohl, P.; Berlinguette, C. P. Spectroscopic detection of halogen bonding resolves dye regeneration in the dye-sensitized solar cell. *Nat. Commun.* **2017**, *8*, 1761.

(22) Swords, W. B.; Simon, S. J.; Parlane, F. G.; Dean, R. K.; Kellett, C. W.; Hu, K.; Meyer, G. J.; Berlinguette, C. P. Evidence for Interfacial Halogen Bonding. *Angew. Chem., Int. Ed.* **2016**, *55*, 5956−5960.

(23) Simon, S. J. C.; Parlane, F. G. L.; Swords, W. B.; Kellett, C. W.; Du, C.; Lam, B.; Dean, R. K.; Hu, K.; Meyer, G. J.; Berlinguette, C. P. Halogen Bonding Promotes Higher Dye-Sensitized Solar Cell Photovoltages. *J. Am. Chem. Soc.* **2016**, *138*, 10406−10409.

(24) Jeon, J.; Park, Y. C.; Han, S. S.; Goddard, W. A., III; Lee, Y. S.; Kim, H. Rapid Dye Regeneration Mechanism of Dye-Sensitized Solar Cells. *J. Phys. Chem. Lett.* **2014**, *5*, 4285−4290.

(25) Robson, K. C.; Hu, K.; Meyer, G. J.; Berlinguette, C. P. Atomic level resolution of dye regeneration in the dye-sensitized solar cell. *J. Am. Chem. Soc.* **2013**, *135*, 1961−1971.

(26) Nugegoda, D.; Hunt, L. A.; Devdass, A.; Cheema, H.; Fortenberry, R. C.; Jurss, J. W.; Hammer, N. I.; Delcamp, J. H. Lewis Acid-Lewis Base Interactions Promote Fast Interfacial Electron Transfers with a Pyridine-Based Donor Dye in Dye-Sensitized Solar Cells. *ACS Appl. Energy Mater.* **2022**, *5*, 1516−1527.

(27) Gao, P.; Kim, Y. J.; Yum, J.-H.; Holcombe, T. W.; Nazeeruddin, M. K.; Grätzel, M. Facile synthesis of a bulky BPTPA donor group suitable for cobalt electrolyte based dye sensitized solar cells. *J. Mater. Chem. A* **2013**, *1*, 5535−5544.

(28) Zhang, B.; Sun, L. Artificial photosynthesis: opportunities and challenges of molecular catalysts. *Chem. Soc. Rev.* **2019**, *48*, 2216−2264.

(29) Dalle, K. E.; Warnan, J.; Leung, J. J.; Reuillard, B.; Karmel, I. S.; Reisner, E. Electro- and Solar-Driven Fuel Synthesis with First Row Transition Metal Complexes. *Chem. Rev.* **2019**, *119*, 2752−2875.

(30) Francke, R.; Schille, B.; Roemelt, M. Homogeneously Catalyzed Electroreduction of Carbon Dioxide-Methods, Mechanisms, and Catalysts. *Chem. Rev.* **2018**, *118*, 4631−4701.

(31) Ji, J. M.; Zhou, H.; Eom, Y. K.; Kim, C. H.; Kim, H. K. 14.2% Efficiency Dye-Sensitized Solar Cells by Co-sensitizing Novel Thieno[3,2-b]indole-Based Organic Dyes with a Promising Porphyrin Sensitizer. *Adv. Energy Mater.* **2020**, *10*, 2000124.

(32) Kakiage, K.; Aoyama, Y.; Yano, T.; Oya, K.; Fujisawa, J. I.; Hanaya, M. Highly-efficient dye-sensitized solar cells with collaborative sensitization by silyl-anchor and carboxy-anchor dyes. *Chem. Commun.* **2015**, *51*, 15894−15897.

(33) Kakiage, K.; Aoyama, Y.; Yano, T.; Otsuka, T.; Kyomen, T.; Unno, M.; Hanaya, M. An achievement of over 12% efficiency in an organic dye-sensitized solar cell. *Chem. Commun.* **2014**, *50*, 6379−6381.
(34) Tsao, H. N.; Yi, C.; Moehl, T.; Yum, J. H.; Zakeeruddin, S. M.; Nazeeruddin, M. K.; Grätzel, M. Cyclopentadithiophene bridged donor-acceptor dyes achieve high power conversion efficiencies in dye-sensitized solar cells based on the tris-cobalt bipyridine redox couple. *ChemSusChem* **2011**, *4*, 591−594.
(35) Ahmad, S.; Bessho, T.; Kessler, F.; Baranoff, E.; Frey, J.; Yi, C.; Gratzel, M.; Nazeeruddin, M. K. A new generation of platinum and iodine free efficient dye-sensitized solar cells. *Phys. Chem. Chem. Phys.* **2012**, *14*, 10631−10639.
(36) Cao, Y.; Saygili, Y.; Ummadisingu, A.; Teuscher, J.; Luo, J.; Pellet, N.; Giordano, F.; Zakeeruddin, S. M.; Moser, J. E.; Freitag, M.; Hagfeldt, A.; Gratzel, M. 11% efficiency solid-state dye-sensitized solar cells with copper(II/I) hole transport materials. *Nat. Commun.* **2017**, *8*, 15390.
(37) Gabrielsson, E.; Ellis, H.; Feldt, S.; Tian, H.; Boschloo, G.; Hagfeldt, A.; Sun, L. Convergent/Divergent Synthesis of a Linker-Varied Series of Dyes for Dye-Sensitized Solar Cells Based on the D35 Donor. *Adv. Energy Mater.* **2013**, *3*, 1647−1656.
(38) Figueira-Duarte, T. M.; Mullen, K. Pyrene-based materials for organic electronics. *Chem. Rev.* **2011**, *111*, 7260−7314.
(39) Zhang, L.; Yang, X.; Wang, W.; Gurzadyan, G. G.; Li, J.; Li, X.; An, J.; Yu, Z.; Wang, H.; Cai, B.; Hagfeldt, A.; Sun, L. 13.6% Efficient Organic Dye-Sensitized Solar Cells by Minimizing Energy Losses of the Excited State. *ACS Energy Lett.* **2019**, *4*, 943−951.
(40) Mathew, S.; Yella, A.; Gao, P.; Humphry-Baker, R.; Curchod, B. F.; Ashari-Astani, N.; Tavernelli, I.; Rothlisberger, U.; Nazeeruddin, M. K.; Grätzel, M. Dye-Sensitized Solar Cells with 13% Efficiency Achieved Through the Molecular Engineering of Porphyrin Sensitizers. *Nat. Chem.* **2014**, *6*, 242−247.
(41) Li, R.; Liu, J.; Cai, N.; Zhang, M.; Wang, P. Synchronously Reduced Surface States, Charge Recombination, and Light Absorption Length for High-Performance Organic Dye-Sensitized Solar Cells. *J. Phys. Chem. B* **2010**, *114*, 4461−4464.
(42) Hagfeldt, A.; Boschloo, G.; Sun, L.; Kloo, L.; Pettersson, H. Dye-Sensitized Solar Cells. *Chem. Rev.* **2010**, *110*, 6595−6663.
(43) Feldt, S. M.; Gibson, E. A.; Gabrielsson, E.; Sun, L.; Boschloo, G.; Hagfeldt, A. Design of Organic Dyes and Cobalt Polypyridine Redox Mediators for High-Efficiency Dye-Sensitized Solar Cells. *J. Am. Chem. Soc.* **2010**, *132*, 16714−16724.
(44) Garcia-Rodriguez, R.; Jiang, R.; Canto-Aguilar, E. J.; Oskam, G.; Boschloo, G. Improving the mass transport of copper-complex redox mediators in dye-sensitized solar cells by reducing the inter-electrode distance. *Phys. Chem. Chem. Phys.* **2017**, *19*, 32132−32142.
(45) Zhang, R.; Zhao, Y.; Li, G.; Yang, D.; Ni, Z. A New Series of Pyrenyl-Based Triarylamines: Synthesis, Structure, Optical Properties, Electrochemistry, and Electroluminescence. *RSC Adv.* **2016**, *6*, 9037−9048.
(46) Karsten, B. P.; Bijleveld, J. C.; Viani, L.; Cornil, J.; Gierschner, J.; Janssen, R. A. J. Electronic structure of small band gap oligomers based on cyclopentadithiophenes and acceptor units. *J. Mater. Chem.* **2009**, *19*, 5343−5350.
(47) Singh, V.; Sharma, K.; Shankar, B.; Awasthi, S. K.; Gupta, R. D. Heteroleptic Cu(II)-polypyridyl complexes as photonucleases. *New J. Chem.* **2016**, *40*, 5906−5913.
(48) Aroua, S.; Todorova, T. K.; Hommes, P.; Chamoreau, L. M.; Reissig, H. U.; Mougel, V.; Fontecave, M. Synthesis, Characterization, and DFT Analysis of Bis-Terpyridyl-Based Molecular Cobalt Complexes. *Inorg. Chem.* **2017**, *56*, 5930−5940.
(49) Roy, S.; Roy, S.; Saha, S.; Majumdar, R.; Dighe, R. R.; Jemmis, E. D.; Chakravarty, A. R. Cobalt(II) complexes of terpyridine bases as photochemotherapeutic agents showing cellular uptake and photocytotoxicity in visible light. *Dalton Trans.* **2011**, *40*, 1233−1242.
(50) Curiac, C.; Hunt, L. A.; Sabuj, M. A.; Li, Q.; Baumann, A.; Cheema, H.; Zhang, Y.; Rai, N.; Hammer, N. I.; Delcamp, J. H. Probing Interfacial Halogen-Bonding Effects with Halogenated Organic Dyes and a Lewis Base-Decorated Transition Metal-Based Redox Shuttle at a Metal Oxide Interface in Dye-Sensitized Solar Cells. *J. Phys. Chem. C* **2021**, *125*, 17647−17659.
(51) Constable, E. C.; Harris, K.; Housecroft, C. E.; Neuburger, M.; Zampese, J. A. Turning {M(tpy)2}n+ embraces and CH···π interactions on and off in homoleptic cobalt(II) and cobalt(III) bis(2,2′:6′,2″-terpyridine) complexes. *CrystEngComm* **2010**, *12*, 2949−2961.
(52) Wallace, A. M.; Curiac, C.; Delcamp, J. H.; Fortenberry, R. C. Accurate determination of the onset wavelength (λonset) in optical spectroscopy. *J. Quant. Spectrosc. Radiat. Transfer* **2021**, *265*, 107544.
(53) Urbani, M.; Grätzel, M.; Nazeeruddin, M. K.; Torres, T. Meso-Substituted Porphyrins for Dye-Sensitized Solar Cells. *Chem. Rev.* **2014**, *114*, 12330−12396.
(54) Anderson, A. Y.; Barnes, P. R. F.; Durrant, J. R.; O'Regan, B. C. Quantifying Regeneration in Dye-Sensitized Solar Cells. *J. Phys. Chem. C* **2011**, *115*, 2439−2447.
(55) Ronca, E.; Pastore, M.; Belpassi, L.; Tarantelli, F.; De Angelis, F. Influence of the dye molecular structure on the TiO_2 conduction band in dye-sensitized solar cells: disentangling charge transfer and electrostatic effects. *Energy Environ. Sci.* **2013**, *6*, 183−193.
(56) Tułodziecki, M.; Leverick, G. M.; Amanchukwu, C. V.; Katayama, Y.; Kwabi, D. G.; Bardé, F.; Hammond, P. T.; Shao-Horn, Y. The role of iodide in the formation of lithium hydroxide in lithium-oxygen batteries. *Energy Environ. Sci.* **2017**, *10*, 1828−1842.
(57) Saygili, Y.; Soderberg, M.; Pellet, N.; Giordano, F.; Cao, Y.; Munoz-Garcia, A. B.; Zakeeruddin, S. M.; Vlachopoulos, N.; Pavone, M.; Boschloo, G.; Kavan, L.; Moser, J. E.; Gratzel, M.; Hagfeldt, A.; Freitag, M. Copper Bipyridyl Redox Mediators for Dye-Sensitized Solar Cells with High Photovoltage. *J. Am. Chem. Soc.* **2016**, *138*, 15087−15096.
(58) Rodrigues, R. R.; Cheema, H.; Delcamp, J. H. A High Voltage Molecular Engineered Organic Sensitizer-Iron Redox Shuttle Pair: 1.4 V DSC and 3.3 V SSM-DSC Devices. *Angew. Chem., Int. Ed.* **2018**, *57*, 5472−5476.
(59) Zeng, K.; Chen, Y.; Zhu, W. H.; Tian, H.; Xie, Y. Efficient Solar Cells based on Concerted Companion Dyes Containing Two Complementary Components: An Alternative Approach for Cosensitization. *J. Am. Chem. Soc.* **2020**, *142*, 5154−5161.
(60) Kohlrausch, R. Theorie des elektrischen Rückstandes in der Leidener Flasche. *Ann. Phys. (Pogg.)* **1854**, *167*, 179−214.
(61) Williams, G.; Watts, D. C. Non-Symmetrical Dielectric Relaxation Behaviour Arising from a Simple Empirical Decay Function. *Trans. Faraday Soc.* **1970**, *66*, 80−85.
(62) Casarin, L.; Swords, W. B.; Caramori, S.; Bignozzi, C. A.; Meyer, G. J. Rapid Static Sensitizer Regeneration Enabled by Ion Pairing. *Inorg. Chem.* **2017**, *56*, 7324−7327.
(63) Lukichev, A. Physical meaning of the stretched exponential Kohlrausch function. *Phys. Lett. A* **2019**, *383*, 2983−2987.
(64) Li, F.; Jennings, J. R.; Wang, Q. Determination of sensitizer regeneration efficiency in dye-sensitized solar cells. *ACS Nano* **2013**, *7*, 8233−8242.
(65) Yang, J.; Ganesan, P.; Teuscher, J.; Moehl, T.; Kim, Y. J.; Yi, C.; Comte, P.; Pei, K.; Holcombe, T. W.; Nazeeruddin, M. K.; Hua, J.; Zakeeruddin, S. M.; Tian, H.; Grätzel, M. Influence of the Donor Size in D-pi-A Organic Dyes for Dye-Sensitized Solar Cells. *J. Am. Chem. Soc.* **2014**, *136*, 5722−5730.
(66) Chen, D. Y.; Hsu, Y. Y.; Hsu, H. C.; Chen, B. S.; Lee, Y. T.; Fu, H.; Chung, M. W.; Liu, S. H.; Chen, H. C.; Chi, Y.; Chou, P. T. Organic dyes with remarkably high absorptivity; all solid-state dye sensitized solar cell and role of fluorine substitution. *Chem. Commun.* **2010**, *46*, 5256−5258.
(67) Zhang, W.; Wu, Y.; Bahng, H. W.; Cao, Y.; Yi, C.; Saygili, Y.; Luo, J.; Liu, Y.; Kavan, L.; Moser, J.-E.; Hagfeldt, A.; Tian, H.; Zakeeruddin, S. M.; Zhu, W.-H.; Grätzel, M. Comprehensive control of voltage loss enables 11.7% efficient solid-state dye-sensitized solar cells. *Energy Environ. Sci.* **2018**, *11*, 1779−1787.
(68) Boschloo, G.; Häggman, L.; Hagfeldt, A. Quantification of the Effect of 4-tert-Butylpyridine Addition to I-/I3- Redox Electrolytes in

https://doi.org/10.1021/acs.energyfuels.2c00633
Energy Fuels 2022, 36, 7075−7086

Dye-Sensitized Nanostructured TiO_2 Solar Cells. *J. Phys. Chem. B* **2006**, *110*, 13144−13150.
(69) Nissfolk, J.; Fredin, K.; Hagfeldt, A.; Boschloo, G. Recombination and Transport Processes in Dye-Sensitized Solar Cells Invetigated under Working Conditions. *J. Phys. Chem. B* **2006**, *110*, 17715−17718.
(70) Cho, I.; Dheendayal, M.; Wagner, P.; Mozer, A. J. Enhanced interfacial electron transfer kinetics between Co(2+/3+) complexes and organic dyes with free space near their backbone. *Phys. Chem. Chem. Phys.* **2022**, *24*, 11183−11195.
(71) Houle, F. A. Adaptive response by an electrolyte: resilience to electron losses in a dye-sensitized porous photoanode. *Chem. Sci.* **2021**, *12*, 6117−6128.
(72) Connelly, N. G.; Geiger, W. E. Chemical Redox Agents for Organometallic Chemistry. *Chem. Rev.* **1996**, *96*, 877−910.
(73) *Handbook of Physics and Chemistry*, 63rd ed.; CRC: Boca Raton, FL, 1982.
(74) Rodrigues, R. R.; Lee, J. M.; Taylor, N. S.; Cheema, H.; Chen, L.; Fortenberry, R. C.; Delcamp, J. H.; Jurss, J. W. Copper-based redox shuttles supported by preorganized tetradentate ligands for dye-sensitized solar cells. *Dalton Trans.* **2020**, *49*, 343−355.
(75) Ellis, H.; Vlachopoulos, N.; Häggman, L.; Perruchot, C.; Jouini, M.; Boschloo, G.; Hagfeldt, A. PEDOT counter electrodes for dye-sensitized solar cells prepared by aqueous micellar electrodeposition. *Electrochim. Acta* **2013**, *107*, 45−51.

https://doi.org/10.1021/acs.energyfuels.2c00633
Energy Fuels 2022, 36, 7075−7086